International Journal of Heat and Mass Transfer 217 (2023) 124614

Contents lists available at ScienceDirect

International Journal of Heat and Mass Transfer

journal homepage: www.elsevier.com/locate/ijhmt

A methodology for measuring heat transfer coefficient and self-similarity of thermal regulation in microvascular material systems

Urmi Devi [a,1], Sandeep R. Kumar [b,1], Kalyana B. Nakshatrala [c], Jason F. Patrick [a,b,*]

[a] Department of Civil, Construction, and Environmental Engineering, North Carolina State University, 27695, Raleigh, USA
[b] Department of Mechanical and Aerospace Engineering, North Carolina State University, 27695, Raleigh, USA
[c] Department of Civil Engineering, University of Houston, 77204, Houston, USA

ARTICLE INFO

Keywords:
Heat transfer coefficient
Active cooling
Microvasculature
Thermophysical properties

ABSTRACT

Fluid transport through microvascular networks—a hallmark for homeostasis in living systems—has transcended to engineered materials, primarily made possible because of modern manufacturing advancements. Vascular-enabled multifunctionality, including thermal regulation and self-healing, holds great potential for extending the lifetime of structural materials and expanding the operational envelope. Prior studies on vascular-based active cooling use a "combined" heat transfer coefficient (HTC): a single parameter lumps convection and radiation effects. Although the resulting mathematical models are linear—an attractive feature for computational modeling, the combined coefficient approach may not be accurate or even applicable if the operating temperature is unknown, which is the case with many thermal regulation applications (e.g., space probes). In this paper, we illustrate the remarked limitations of the lumped approach and advocate the need to use a decoupled HTC by splitting convective and radiative heat transfer modes. We show the broad applicability of the proposed method by applying it to three material systems: glass and carbon fiber-reinforced polymer composites and an additive manufactured metal. We show, using numerical simulations, the differences in the predictions from the decoupled approach with that of the combined HTC; these differences are prominent at higher heat fluxes. Also, the decoupling has enabled us to establish a scaling law that allows transferring of solutions fields across material systems, strengthening further the validity and utility of our approach. This work's significance is two-fold. *First*, the research is fundamental, providing accurate measurement protocols for critical model parameters. *Second*, this work facilitates the development of mathematical models for vascular-based thermal regulation that are predictive even for hostile environments (which are often difficult to realize in laboratories), such as outer space.

1. Introduction

Bioinspired "active cooling" via liquid circulation through internal vasculature is able to protect polymer-matrix fiber-composites and also devices housed by these lightweight structural materials from overheating [1,2]. Such cooling systems have immediate relevance in aerospace structures (e.g., satellites) that are subject to intense and erratic thermal environments [3–5]. For instance, active cooling of photovoltaic panels on the Parker solar probe has been a vital factor in enabling the closest pass to the sun ever to be made, during which the heat flux on solar panels reached as high as 4,500 W/m^2 [4]. Under such drastic conditions and even in less demanding thermal transport scenarios such as Li-ion batteries that experience heat fluxes an order of magnitude lower ($\approx$ 500 W/m^2) [6], accurate analytical/numerical modeling with experimentally derived inputs are necessary to properly capture the underlying behavior and provide suitable design guidance.

To this end, a number of high-fidelity models are employed, which often come with large computational overhead that limits their utility to simple domains. On the other hand, reduced order models (ROMs) provide computationally efficient alternatives [7–9], especially for slender structures [10,11]. Our recent study [12] using one such ROM to investigate the thermal behavior of thin vascular plates showed good qualitative agreement with experimental results, while indicating a scope for improvement on the quantitative front. Here we sought to better under-

* Corresponding author at: Department of Civil, Construction, and Environmental Engineering, North Carolina State University, 27695, Raleigh, USA.
E-mail address: jfpatric@ncsu.edu (J.F. Patrick).
[1] These authors contributed equally to this work.

https://doi.org/10.1016/j.ijheatmasstransfer.2023.124614
Received 28 May 2023; Received in revised form 25 July 2023; Accepted 18 August 2023
Available online 13 September 2023

stand whether the difference between experimental and ROM results is due to a lack of capturing the actual physics, inaccurate measurements of material/system properties, or a combination thereof.

One area of particular focus relates to a coupled/combined convective and radiative heat transfer coefficient (HTC). The governing equation resulting from the use of a combined HTC is linear with respect to the temperature difference (ΔT) between average surface and ambient values. This simplifies numerical simulations to a linear problem as opposed to requiring a nonlinear iterative solution strategy that is computationally more costly. While the simplifying strategy has merit for more quickly producing optimized vascular designs [13–16], the assumption of a combined HTC is philosophically inconsistent with Newton's law of cooling that states convective heat transfer does not vary (i.e., remains constant) with respect to ΔT [17–19]. Under certain conditions, such as lower temperatures, a combined HTC may be suitable for capturing the thermal response. However, in other situations where high temperatures are involved or when radiation is the primary mode of heat transfer (e.g., solar radiation in the vacuum of outer space [20,21]), a combined HTC might be a poor choice for analysis. Here the nonlinear Stefan-Boltzmann law will govern the thermal behavior where temperature raised to the fourth power can result in predictions far from physical reality for simulations that simply combine heat transfer modes/coefficients [22].

For the microvascular conjugate-heat transfer problem that we are particularly interested in, there are multiple modes of thermal transport simultaneously at play in addition to natural convection and radiation from the exposed surfaces. These include conduction through the bulk of the solid and advection to the coolant circulating through the vasculature [12]. The advective heat transfer involves forced convection where heat is extracted from the inner wall of the vasculature to the coolant that is circulated within. This mode also brings in additional scaling effects such as viscous dissipation and axial conduction arising from the temperature gradient along the length of the vasculature [23,24]. The ROM used in this study, however, simplifies the three-dimensional channel to a one-dimensional line element, thereby also eliminating associated scaling effects for the problem that could arise due to boundary layer effects within the channel [10]. Instead, heat transfer to the coolant is accounted for by its mass flow rate, specific heat and temperature rise across the inlet and outlet orifices of the channel. The convective HTC referred to in this paper, therefore, pertains to the natural convention between the exposed surface of the host solid and the external flow of ambient air around it.

To account for this natural convection, two approaches are commonly used in heat transfer. The first is an empirical approach that utilizes dimensionless numbers to correlate fluid flow conditions to the geometric configuration of the solid [25]. These correlations are mostly restricted to simple geometries such as plates, fins, and channels [26–28]. The second approach is through the use of a model popularly known as Newton's law of cooling [29], which uses an average parameter—the convective HTC (h_{conv})—to account for the respective heat exchange process. Calculating h_{conv} requires the free stream temperature of the fluid outside the boundary layer thickness (ambient temperature in this case) as well as the surface temperature of the solid [30]. When direct measurement of surface temperature is not possible, an alternate formulation of the model such as the Wilson plot method is used [31,32]. This alternative does not require surface temperature as a direct input, but uses a secondary descriptor such as thermal resistance to compute h_{conv}. While accurate calculation of HTCs accounting for all these factors continues to be an active area of research [33,34], various probing techniques have also been developed on the experimental front for direct/indirect measurement of solid surface temperatures.

The suitability of a probing technique for a given problem depends broadly on the geometry of the heat transfer surface, its accessibility to temperature measurement and the fluid flow conditions involved. During measurements, care must be taken not to disturb the flow field or to introduce additional heat transfer modes through the sensors, leads, etc. Where the geometry of the host solid is visually accessible, optical methods are well suited to capture the temperature field with high fidelity. Optical methods have evolved from using interferometric fringes in the visible light spectrum as early as the 20th century [35] to more modern techniques, including laser interferometry [36] and infrared (IR) thermography [37].

IR thermography has been successfully employed over the past few decades for flow visualization [38,39] as well as for the measurement of surface temperatures to estimate h_{conv} for a variety of geometries and flow conditions [40,41]. The technique is known for its ability to accurately measure temperature on a two-dimensional surface, making it well-suited to capture spatial distribution of the temperature field for an actively-cooled plate. IR imaging also has the advantage of fast response times (as low as 20 μs), making it ideal for capturing temporal variations in the temperature field and hence also tracking thermal evolution through the transient regime into steady state [37]. The flat plate geometry of the test specimens utilized in this study, and also prior active-cooling investigations [2,12,13,42,43], makes IR thermography an ideal measurement platform.

Synthesizing theory and measurement approaches with the goal of accurate and predictive modeling, here we have developed a practical methodology for decoupling convective and radiative heat transfer on the exterior surface of actively-cooled vascular fiber composite and metal plates. We study such aspects using a variety of state-of-the-art vascular material platforms (i.e., fiber-reinforced polymer composites and additively manufactured metal) to evaluate the broad applicability of our approach. Moreover, we compare and validate numerical results and assess the capabilities of our new paradigm for predictive simulations beyond conditions that cannot be easily replicated in the laboratory. The advancements result in better predictions from simulations that are consistent with theory, and provide additional clarity to the field of actively-cooled microvascular systems. Spanning an array of materials and heat fluxes, the developed body of knowledge from our study is readily translatable to numerous applications (e.g., electric vehicles, satellites) for finer control and to enhance thermal regulation performance.

An outline for the rest of this article is as follows. Section 2 establishes the motivation for the present work and states our hypothesis. Section 3 lays out the proposed methodology for determining decoupled convective and radiative HTCs compared to the prior combined HTC approach. Section 4 describes active-cooling experiments and compares the behavior with steady-state heat transfer simulations using a reduced-order model (ROM) – for both combined and decoupled HTCs. We also simulate active-cooling performance for applied heat fluxes far outside laboratory capabilities and contrast predictions with differing HTCs. Section 5 presents a dimensional analysis framework for establishing a scaling to transfer the temperature field across material systems, which is only feasible with the decoupled HTC approach. Finally, the main research findings are summarized along with a discussion on potential future research endeavors.

2. Motivation and hypothesis

In this section, we lay out the heat transfer problem and illustrate the issues associated with characterization of thermal regulation in thin flat plates. The collective picture allows us to establish the motivation for this research and state the hypothesis of our proposed approach to determine the heat transfer coefficient (HTC).

2.1. A model active-cooling system

Fig. 1 shows a schematic representation of typical heat transfer modes and boundary conditions encountered in a thin vascular plate that is heated uniformly from below. When the lateral boundaries are insulated, the salient modes of heat transfer include natural convection

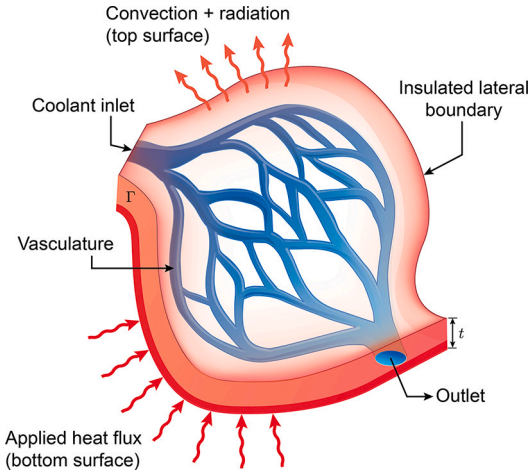

Fig. 1. Schematic of heat transfer modes and boundary conditions in a thin vascular active-cooling system. *Bottom surface*: uniformly applied heat flux. *Top surface*: atmospheric convection plus radiation. *Vasculature*: advective heat transfer by flowing liquid coolant. *Lateral boundary*: insulated (assumed adiabatic).

and radiation from the exposed top surface to the surrounding ambient environment, conduction through the host solid, and advection from the inner wall of the vasculature to the coolant flowing within. In this study, the conduction within the host solid from the heat source to the exposed top surface does not contribute to the heat dissipated from the system to the environment since the system is characterized at steady-state. Advection is accounted for through the heat capacity of the flowing coolant, while other associated scaling effects (e.g., axial conduction within the coolant [24]) are eliminated by the ROM. Consequently, the primary heat transfer modes of interest (aside from advection) are natural convection and radiation from the exposed top surface to the ambient atmosphere, which are investigated for possible sources of discrepancy between experimental and ROM results seen in prior literature [12].

2.2. Convective versus radiative heat transfer

In prior vascular-based active-cooling studies [12,13], the cumulative effect of natural convection and radiation from the exposed top surface (Fig. 1) is described by a combined HTC (h_{comb}). The addition of convective (h_{conv}) and radiative (h_{rad}) HTCs to obtain h_{comb} tacitly absorbs the nonlinearity associated with radiation (detailed in Section 3). This renders h_{comb} nonlinearly dependent on temperature. A visual representation is shown in **Fig. 2a**, where h_{comb} is calculated using typical heat transfer properties for natural convection ($h_{conv} = 13.5$ W/(m^2·K)) and radiation (emissivity, $\epsilon = 0.95$) from a horizontal flat plate top surface to the surrounding air at ambient temperature ($T_{amb} = 22.5$ °C). The surface temperature upon which h_{comb} depends, however, is rarely known a-priori and is generally obtained as an output of the thermal analysis. This leads to the conundrum of selecting the highly temperature-dependent h_{comb} without knowledge of the temperature to be encountered in the analysis. The convective HTC (h_{conv}) on the other hand is a temperature-independent quantity that can be used to faithfully account for the convective process across a broader range of operating temperatures. Radiative effects, when present, must then be accounted for by a separate radiative HTC (h_{rad}) to obtain the most accurate results. Fig. 2b indicates that radiative effects are not negligible even at the lowest applied heat fluxes within the range of 200 to 1000 W/m^2. Under such conditions, radiation accounts for nearly 33% of the total heat transfer from the exposed top surface where convection is responsible for the remaining portion. While computationally more demanding and requiring an iterative nonlinear solution strategy, the approach of decoupling convective and radiative heat transfer is more accurate and therefore better suited for predictions.

2.3. Spatial variation of top surface temperature

While knowing the operating temperature in a specific application may help in selecting a reasonable value of h_{comb} for thermal analysis, the temperature field may not be uniform over the entire surface. **Fig. 3** shows the "hot steady-state" (HSS) spatial temperature distributions of the exposed top surface obtained from IR thermography for four structural materials with increasing thermal conductivity: glass-fiber reinforced polymer composite (GFRP), carbon-fiber-reinforced polymer composite (CFRP), a nickel-chromium metal alloy (In718), and nearly pure copper (Cu110). The HSS temperature contours are obtained for applied heat fluxes of 200, 1000 and 2000 W/m^2 as detailed in Section A.1. Probability density function (PDF) plots indicate that temperature uniformity is difficult to achieve even within controlled laboratory conditions, with less uniformity in lower thermal conductivity materials and for the higher applied heat fluxes. The surface temperature in specific real-world applications (e.g., space probes) could also vary by orders of magnitude due to operating conditions. Thus, using h_{comb} can lead to incorrect predictions since, at higher temperature ranges, the value of the combined HTC can vary greatly even for minor variations in surface temperature, as evidenced by Fig. 2a. Therefore, even if the operating temperatures are known a priori, h_{comb} may not be an accurate choice for the entire surface. In contrast, h_{conv} is theoretically constant for a given set of surface geometry and fluid flow conditions, whereby a value of h_{conv} obtained from a particular heat flux regime can therefore serve as a reasonable estimate for a different heat flux case. The convective HTC can then be used in conjunction with h_{rad} for accurate thermal analysis even with spatially varying temperature fields.

To summarize: (i) the combined heat transfer coefficient depends nonlinearly on the operating temperature (which is often unknown in real-world applications), (ii) the contribution from radiation is significant compared to convection, (iii) maintaining uniform spatial temperature is difficult to achieve at higher heat fluxes and especially for materials with low thermal conductivity. Ergo, we presuppose that splitting the convective and radiative components and quantifying these heat transfer contributions at low applied fluxes (possible in laboratories) will provide accurate predictions across various real-world scenarios.

3. A methodology for decoupling heat transfer coefficients (HTCs)

In this section, we first describe the methodology to calculate the combined HTC (h_{comb}) that is common to prior thermal regulation studies [12,13,44]. Then we provide an approach to decouple the convective (h_{conv}) and radiative (h_{rad}) HTCs, and compare the results from this approach to those obtained from the combined HTC method.

In the absence of vascular fluid flow within our model thermal regulation system (Fig. 1) with insulated (i.e., adiabatic) lateral boundaries, the heat flux entering the system is conducted through the solid to the exposed top surface. When the system reaches steady-state (i.e., the top surface temperature no longer changes), calculating the combined HTC involves a thermal energy balance equating the supplied heat flux (q_{in}) entering the system to the sum of convective (q_{conv}) and radiative (q_{rad}) heat fluxes exiting the top surface, as provided below:

$$q_{in} = q_{conv} + q_{rad}. \tag{1}$$

Here, q_{conv} and q_{rad} can be expressed based on Newton's law of cooling (Equation (2)) and the Stefan-Boltzmann law (Equation (3)) [18], respectively:

$$q_{conv} = h_{conv}(\overline{T}_{surf} - T_{amb}) = h_{conv}(\Delta T), \tag{2}$$

$$q_{rad} = \epsilon\sigma(\overline{T}^4_{surf} - T^4_{amb}), \tag{3}$$

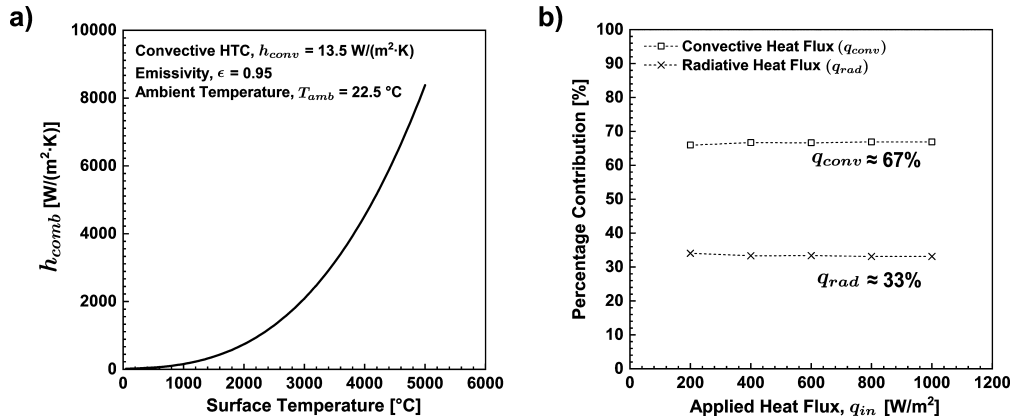

Fig. 2. (a) Representative combined heat transfer coefficient (h_{comb}), i.e., the summation of convective (h_{conv}) and radiative (h_{rad}) HTCs, versus surface temperature. h_{comb} is calculated for fixed values of h_{conv} = 13.5 W/(m²·K) and emissivity (ϵ = 0.95). **(b)** Relative percentage contribution of convective (q_{conv}) and radiative (q_{rad}) heat fluxes to the total applied heat flux (q_{in}).

where, h_{conv} is the convective HTC, ΔT is the difference between the average top surface temperature ($\overline{T}_{surf}$) and ambient temperature (T_{amb}), ϵ is the surface emissivity ($0 \leq \epsilon \leq 1$), and σ is the Stefan–Boltzmann constant ($\sigma = 5.67 \times 10^{-8}$ W/(m^2· K^4)) derived from other physical constants [45].

By expanding Equation (3), we obtain:

$$q_{rad} = \epsilon\sigma(\overline{T}_{surf} - T_{amb})(\overline{T}_{surf} + T_{amb})(\overline{T}^2_{surf} + T^2_{amb}). \tag{4}$$

Factoring out the radiative HTC ($h_{rad} \equiv \epsilon\sigma(\overline{T}_{surf} + T_{amb})(\overline{T}^2_{surf} + T^2_{amb})$), we arrive upon a simplified form of the Stefan-Boltzmann law:

$$q_{rad} = h_{rad}(\overline{T}_{surf} - T_{amb}) = h_{rad}(\Delta T). \tag{5}$$

By substituting q_{conv} and q_{rad} from Equations (2) and (5), respectively, into Equation (1), and neglecting any heat loss through the insulated lateral boundaries, we arrive upon:

$$q_{in} = (h_{conv} + h_{rad})\Delta T, \tag{6}$$

where the combined HTC is merely the summation of convective and radiative HTCs, i.e.,

$$h_{comb} = h_{conv} + h_{rad}. \tag{7}$$

The combined HTC (h_{comb}) is calculated by plotting the applied heat fluxes (q_{in}) against corresponding values of ΔT on the x-axis and then by performing a linear least-squares regression on n such data pairs. The slope of this fitted line represents the combined HTC:

$$h_{comb} = \frac{\sum q_{in}\Delta T - \frac{1}{n}\sum q_{in}\sum \Delta T}{\sum(\Delta T)^2 - \frac{1}{n}(\sum q_{in})^2}. \tag{8}$$

To properly capture the differing underlying physical phenomena and in-turn provide more accurate input for numerical modeling of active-cooling, we have developed a practical methodology to separately calculate the convective and radiative HTCs. A comparative flowchart is provided in **Fig. 4** outlining the key steps of this decoupled approach versus the combined HTC (h_{comb}) calculation.

In both combined and decoupled approaches, first the geometry of the host solid is measured and used to calculate the applied heat flux (q_{in}), a ratio between the supplied heat and the surface area of the plate. In our experiments, heat is generated by a thin-film electrically resistive substrate where the input DC power (i.e., voltage × current) equates to the supplied heat [12,13]. A series of hot steady-state (HSS) experiments are performed at increasing applied heat fluxes. With lateral sides insulated, a prescribed heat flux is applied until the average top surface temperature ($\overline{T}_{surf}$)—measured by an IR camera—reaches steady-state, i.e., herein when the average surface temperature does not vary by more than 0.2 °C over a 10 minute period (see Section A.1). The ambient temperature (T_{amb}) is recorded as the average reading from a thermocouple over the same HSS time interval, which matches the IR camera reading at zero heat flux. Since the temperature readings are taken at steady state, a cool down between ascending heat fluxes is not necessary, which reduces the experimental time demand; cooling to ambient would be required between heat fluxes applied in descending order (see Section A.2).

For the decoupled approach, after reaching HSS, the surface emissivity (ϵ) of each material is determined via calibrating the average top surface temperature with respect to a reference emitter of known emissivity, in accordance with the ASTM standard [46]; see Section A.3 for details. Note that surface emissivity measurements are not necessary to determine the combined HTC (Fig. 4a).

For each applied heat flux (q_{in}), the radiative heat flux (q_{rad}) is calculated by substituting the measured surface emissivity, average top surface temperature, and ambient temperature into the Stefan-Boltzmann law (Equation (3)).

The radiative heat transfer coefficient (h_{rad}) is then calculated by dividing each radiative heat flux (q_{rad}) by the difference in average top surface and ambient temperatures ($\Delta T = \overline{T}_{surf} - T_{amb}$):

$$h_{rad} = q_{rad}/\Delta T. \tag{9}$$

The corresponding convective heat flux (q_{conv}) is then calculated by subtracting the radiative heat flux from the applied heat flux using the thermal energy balance (Equation (1)) without considering any boundary loss.

The convective heat fluxes (q_{conv}) are then plotted against corresponding ΔT values on the x-axis. Similar to the combined HTC, a linear least-squares regression is performed for n pairs of data, where the convective HTC (h_{conv}) is the slope of the fitted line:

$$h_{conv} = \frac{\sum q_{conv}\Delta T - \frac{1}{n}\sum q_{conv}\sum \Delta T}{\sum(\Delta T)^2 - \frac{1}{n}(\sum q_{conv})^2}. \tag{10}$$

To evaluate the versatility of this new decoupling approach, we examine three different plain (i.e., non-vascular) materials with varying thermal properties and material makeup: (i) glass fiber-reinforced epoxy-matrix composite (GFRP), (ii) carbon fiber-reinforced epoxy-matrix composite (CFRP), and (iii) Inconel 718 (In718) nickel-chromium metal alloy. The fiber-composites are anisotropic (i.e., transversely isotropic) and thus, we measure both in-plane and out-of-plane thermal conductivity, respectively: GFRP (0.64 and 0.52 W/(m·K)) and CFRP (3.21 and 0.78 W/(m·K)). We assume that the additively manufactured In718 is isotropic with a thermal conductivity of 11.2 W/(m·K)

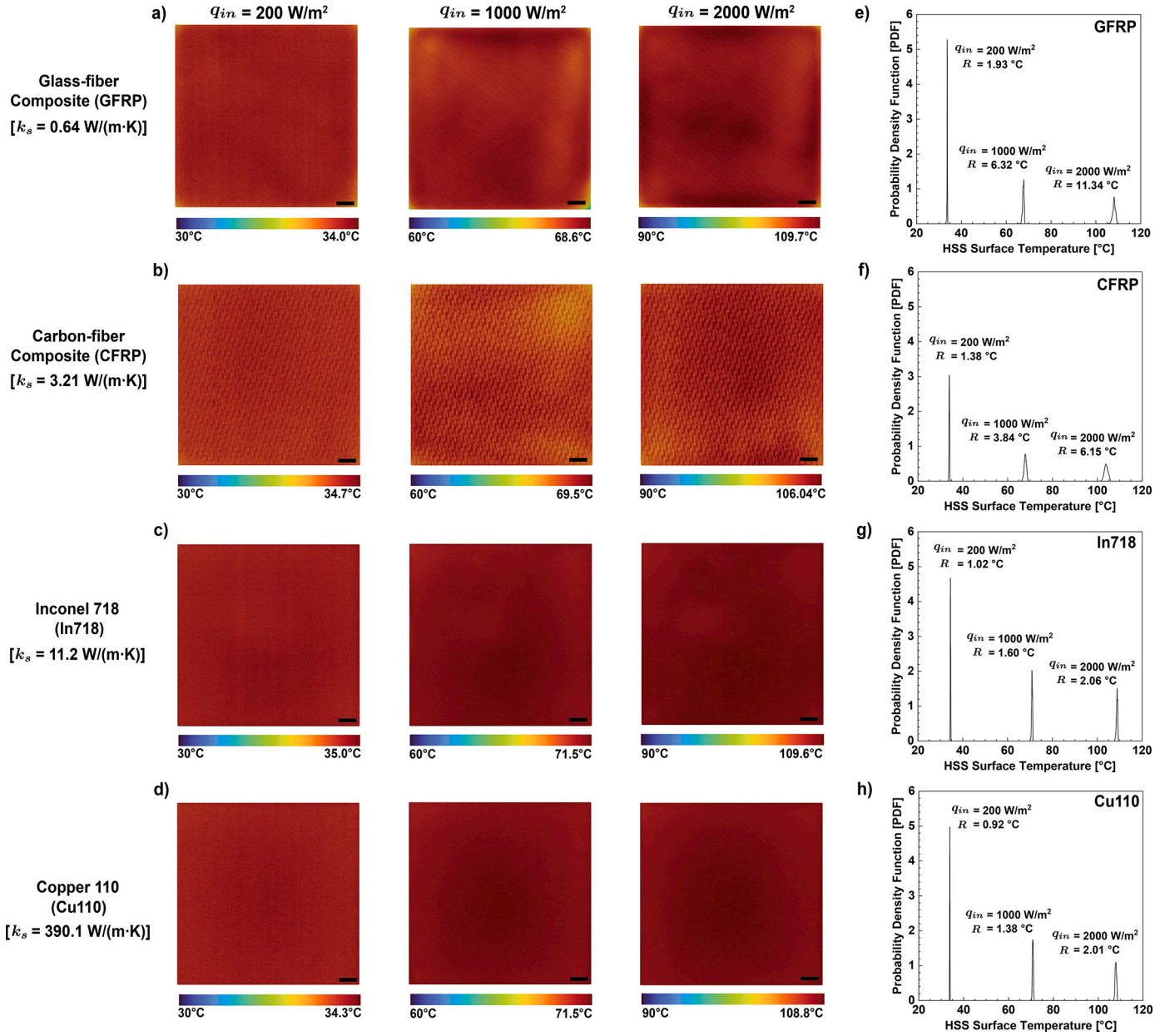

Fig. 3. Hot steady-state (HSS) top surface temperature contours at applied heat fluxes (q_{in}) of 200, 1000, and 2000 W/m^2 in non-vascular thin (≈ 4 mm) plates: **(a)** GFRP, **(b)** CFRP, **(c)** In718, and **(d)** Cu110. (Note: k_s for GFRP and CFRP composites refer to the respective in-plane thermal conductivity values whereas k_s for In718 and Copper110 are the respective isotropic thermal conductivity values). **(e, f, g, h)** Probability density functions (PDFs) from the HSS surface temperature distributions for the four materials where R values represent the range of temperatures at each respective applied heat flux.

according to time-domain thermoreflectance (TDTR) measurements [47]. Since the reduced-order model (ROM) employed in this study considers a 2D solid domain, only in-plane thermal properties are required and tabulated in Table A.1. We conduct HSS experiments at various applied heat fluxes (q_{in}), from 200 to 1000 W/m^2 in 200 W/m^2 increments, which are readily obtained with standard laboratory equipment. A uniform temperature distribution is achieved with a standard deviation of no more than ± 0.3 °C. Since the reflective surfaces of the machined In718 interfere with the IR camera thermal measurements, the top surface is sandblasted followed by painting matte black. Note this results in a top surface emissivity of 0.94 that is similar to unpainted GFRP (0.99) and CFRP (0.97).

The convective HTCs (h_{conv}) obtained from the linear least-squares fit are 14.29, 14.11, and 13.12 W/(m^2·K) for GFRP, CFRP, and In718, respectively (**Fig. 5**). In addition to strong correlation for all regressions ($R^2 > 0.99$), good agreement (within 10%) amongst h_{conv} values for different materials supports the theory that h_{conv} is not a material property, but rather constant with respect to ΔT and dictated by the convective boundary layer across the top surface. The emissivity values for each host material remain nearly constant for increasing heat flux since the experimental range of ΔT is small (< 50°C). We conducted three repeat experiments for each applied heat flux to ensure repeatability in measurements and resulting HTC calculations, for which standard deviations are minimal (< 0.7%) thereby indicating experimental precision (see Fig. A.2). While the data provided in Fig. 5 emanates from plain (i.e., non-vascular materials), we also conducted HSS experiments on GFRP with a closely-spaced (6 mm) serpentine micro-channel at mid-thickness without observing statistically significant differences (≈ 3%) in convective HTC measurements compared to plain GFRP (Section A.4).

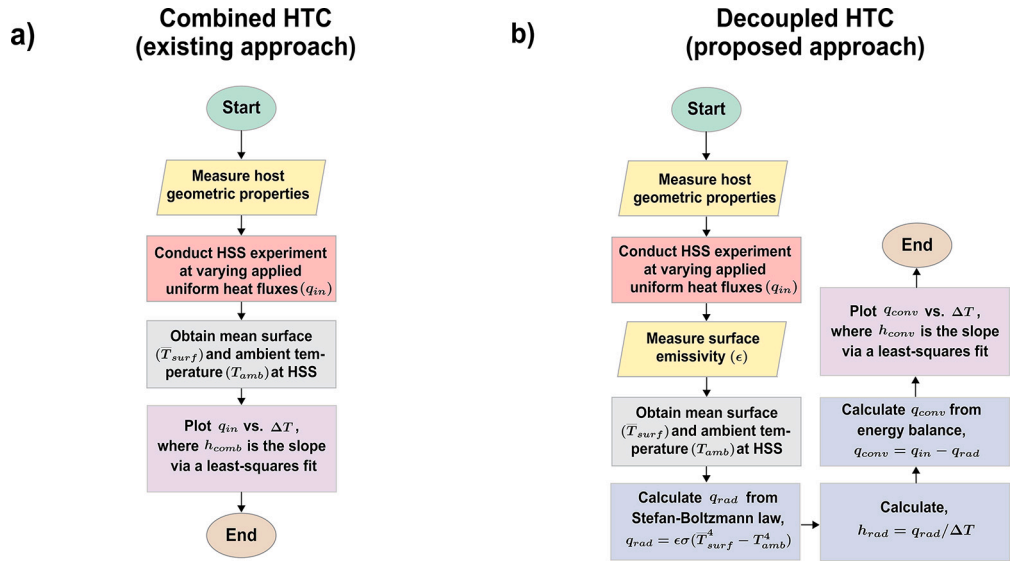

Fig. 4. Heat transfer coefficient (HTC) calculation procedures: **a)** Existing approach to calculate combined HTC (h_{comb}), and **b)** Proposed approach to obtain decoupled convective (h_{conv}) and radiative (h_{rad}) HTCs.

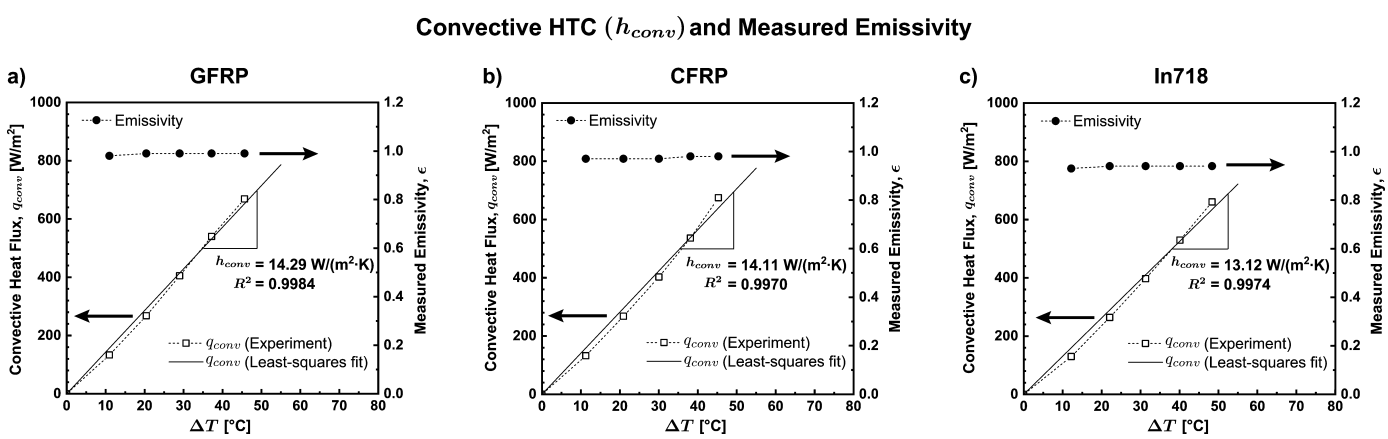

Fig. 5. Convective HTC (h_{conv}) determination from the linear least-squares fit of q_{conv} versus ΔT along with measured emissivity (ϵ) values at five different ΔT (i.e., heat fluxes) for three plain (i.e., non-vascular) materials: **(a)** GFRP, **(b)** CFRP, and **(c)** In718.

4. Active-cooling simulations and experimental validation

To investigate the predictive performance of the proposed HTC decoupling approach, we perform 2D steady-state active cooling simulations in COMSOL® v6.0 across all three materials using a reduced order model (ROM) [10]. We select two vascular designs that represent different flow characteristics: (i) single sinusoidal channel and (ii) branched co-planar network (Sections A.5 and A.6). A distilled water coolant flow rate of 10 mL/min is chosen that is within the laminar flow regime and thus consistent with ROM assumptions. Two sets of numerical simulations are performed, one considering the combined HTC (h_{comb}) and the other including the decoupled convective (h_{conv}) and radiative (h_{rad}) HTCs as inputs to the numerical model. For both sets of simulations, we apply the boundary conditions shown in Fig. 1, including the adiabatic lateral boundary. In addition to HTCs, other simulation input parameters are provided in Table A.1. We perform a series of active cooling simulations with applied heat fluxes ranging from 100 to 15,000 W/m^2, where greater than 2,000 W/m^2 is beyond what is achievable in our laboratory. Modern examples that fall within this applied heat flux range are electric vehicle batteries (500 W/m^2) [6,48], solar probes (4,500 W/m^2) [4], and fuel cells (10,000 W/m^2) [49].

Fig. 6 shows the "cold steady-state" (CSS) top surface temperature contours for all three materials and two vasculatures obtained from the simulations at an applied heat flux of 1,000 W/m^2 (within the laboratory scope) and also 15,000 W/m^2 (well beyond our laboratory capabilities). For both applied heat fluxes, as the host material thermal conductivity increases, the temperature contours become cooler overall and a more uniform temperature distribution is achieved, the latter similar to results in Fig. 3 obtained for non-vascular plates. In718 having the highest thermal conductivity, is able to transfer heat more easily to the coolant within the micro-channel and to the top surface, therefore resulting in the lowest temperature contours with greatest uniformity. Furthermore, at 1,000 W/m^2 there is not a significant difference between the temperature contours obtained from simulations with the combined HTC versus decoupled HTC inputs. On the other hand, for 15,000 W/m^2, there is an observable difference between contours from combined and decoupled HTC simulations, with cooler temperature contours obtained for the decoupled HTC case. The difference between cases is greater for the lower thermal conductivity materials (i.e., GFRP and CFRP) compared to that of the In718 metal with higher thermal conductivity.

To validate these observations, we conduct active-cooling experiments on the three host materials, for both vascular designs, which represent different manufacturing complexity (**Fig. 7**). To fabricate the microvascular FRP composites, we 3D print vascular templates from sacrificial poly(lactic) acid (PLA) [50] and place at the mid-plane of each composite layup. A sinusoidal sacrificial PLA template embedded

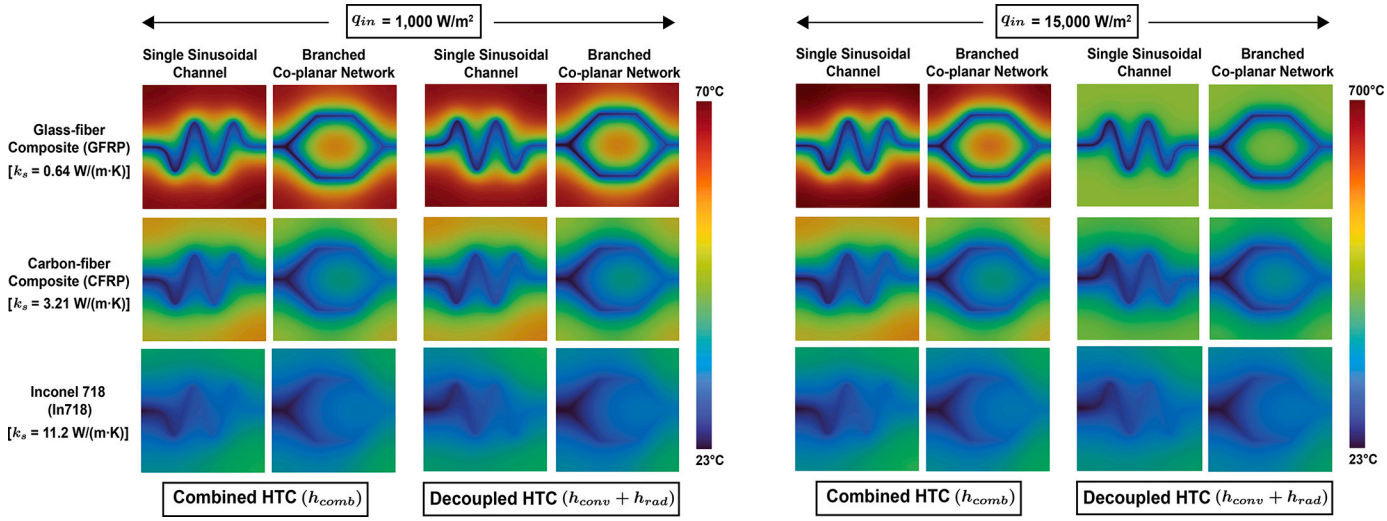

Fig. 6. Cold steady-state (CSS) temperature contours obtained from two sets of simulations, one with a combined HTC (h_{comb}) input and another with the decoupled HTC inputs (h_{conv} and h_{rad}) at applied heat fluxes of 1,000 and 15,000 W/m^2 for all vascular materials/designs. (Note: k_s for GFRP and CFRP composites are respective in-plane thermal conductivity values whereas for In718, k_s is the isotropic thermal conductivity.)

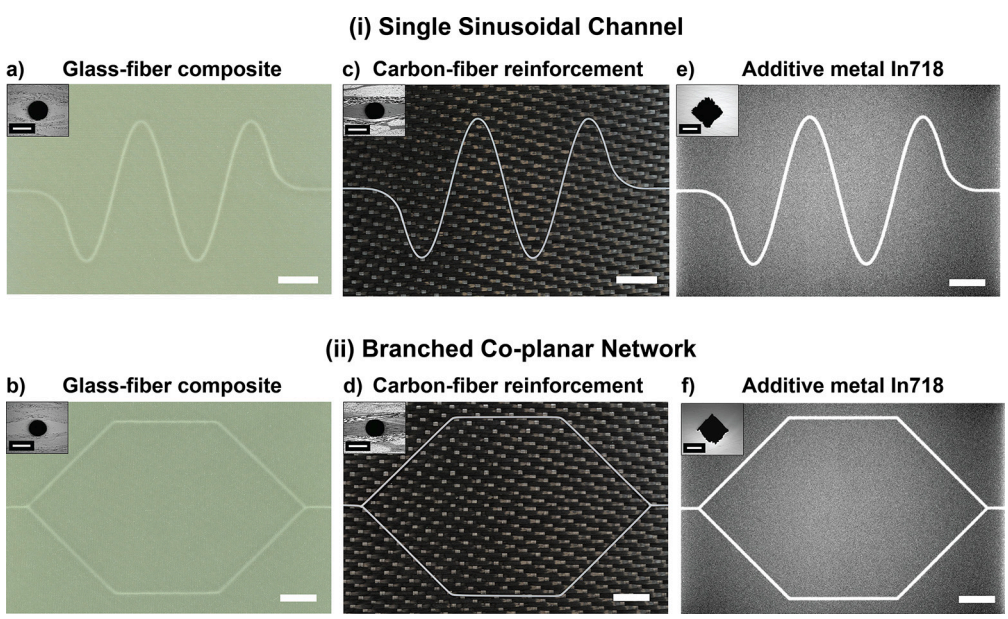

Fig. 7. Active-cooling samples. **(i)** Single sinusoidal channel and **(ii)** branched co-planar network. **(a, b)** Pre-vascularized glass fiber-reinforced polymer (GFRP) composites with embedded 3D printed sacrificial PLA templates. **(c, d)** Sacrificial PLA templates atop woven carbon-fiber reinforcement; zoomed insets showing circular micro-channel cross-sections after vascularization. **(e, f)** Micro-CT reconstruction of the additively manufactured In718 metal; zoomed insets showing diamond-shaped micro-channel cross-sections. (scale bars: *macro images* = 10 mm, *micro images* = 500 μm.)

in GFRP and a branched template atop woven carbon-fiber are shown in Figs. 7a and 7b, respectively. Inverse-replica microvasculature is created via the vaporization of sacrificial components (VaSC) process [51] (see Section A.5). After VaSC, circular cross-section micro-channels are produced with a hydraulic diameter of 500 ± 20 μm.

Both sinusoidal and branched vasculature are also constructed within the nickel-chromium alloy (In718) using a selective laser melting (SLM) process (Section A.6), whereby a high power laser (200 W) melts and fuses metallic powder spread in successive thin layers on top of a build platform [52]. A self-supporting diamond cross-section (same hydraulic diameter to the GFRP/CFRP cylindrical micro-channels) is selected as it retains shape better in the powder state and after SLM than a circular geometry [53]. X-ray computed microtomography (Micro-CT) scans in Figs. 7e and 7f show no channel constrictions or residual metal powder that could obstruct fluid flow.

Active-cooling experiments are conducted at the same coolant flow rate (10 mL/min) as the simulations and ensured to be within laminar regime (see Section A.7). Heat fluxes of 200, 500, 1000, 1500, and 2000 W/m^2 are applied, with the highest flux just within capacity of the DC power supply. Simultaneous heating and active-cooling is performed until reaching the cold steady-state (CSS). The CSS criterion is defined similar to the HSS (i.e., when the average top surface temperature does not change by more than ± 0.2 °C for 10 minutes), except now with coolant flowing through the microchannels. Top surface and ambient temperatures are recorded by an IR camera and thermocouple, respectively. Two additional thermocouples are inserted into the center of the tubing at the inlet and outlet nozzle connections to measure the coolant temperature during the active-cooling experiments.

Fig. 8 compares the average top surface temperatures from active-cooling experiments (up to 2,000 W/m^2 applied heat flux) with results

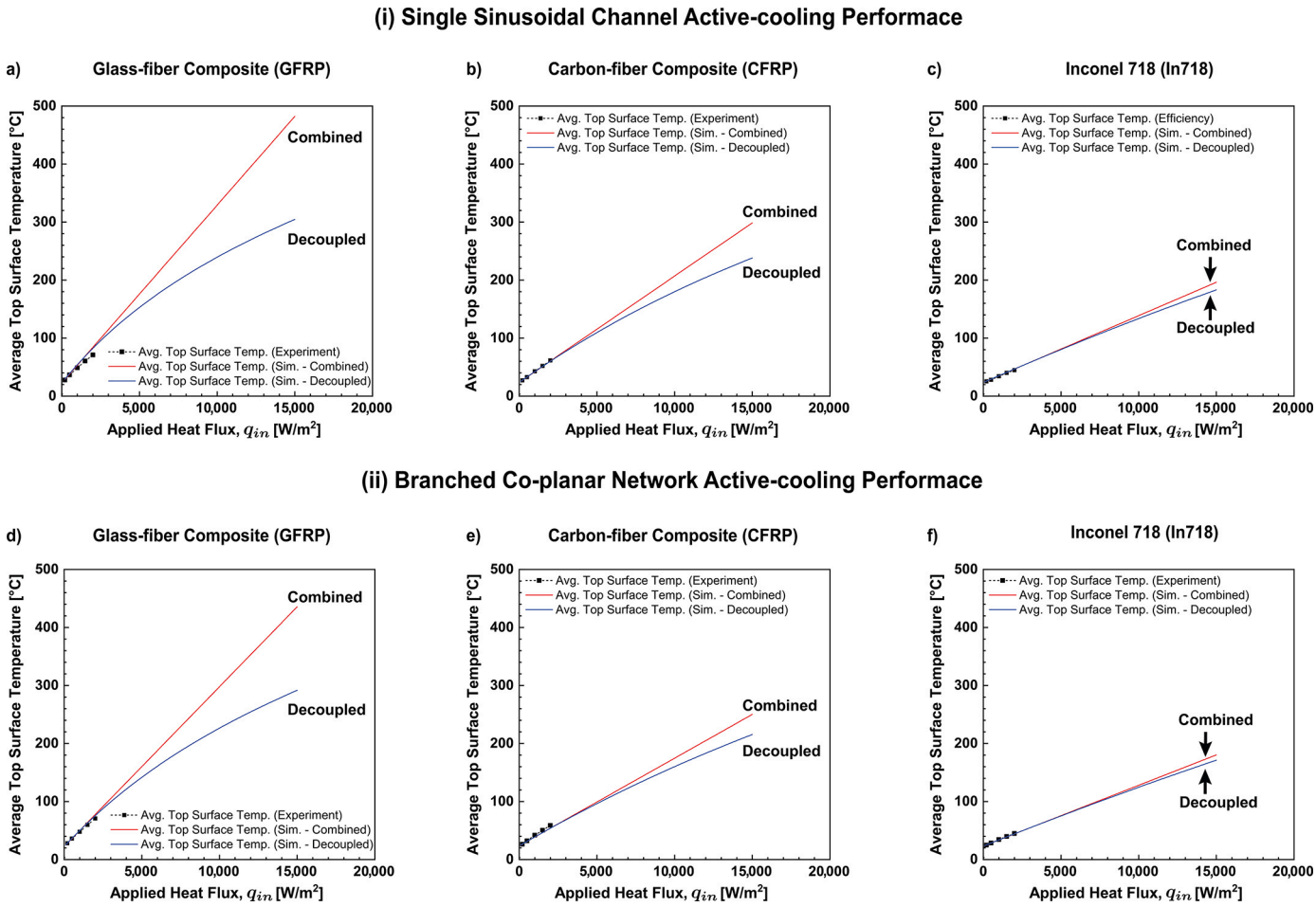

Fig. 8. Active-cooling performance evaluation for both **(i)** single sinusoidal channel and **(ii)** branched co-planar network within **(a, d)** GFRP, **(b, e)** CFRP, and **(c, f)** In718 via comparison of average top surface temperatures at cold steady-state (CSS) obtained from experiments (up to q_{in} = 2,000 W/m^2) and steady-state simulations (up to q_{in} = 15,000 W/m^2) for two cases of HTC input: combined (i.e., h_{comb}) and decoupled (i.e., h_{conv} and h_{rad}).

from the simulations that were conducted up to 15,000 W/m^2. Similar to the simulation temperature contours from Fig. 6—for lower applied heat fluxes—the average top surface temperature resulting from combined and decoupled HTC cases nearly overlap with each other. These closely match the active-cooling experimental results, validating our measurement and model input methodology. As the heat flux increases, however, the average top surface temperature from simulations increases linearly for the combined HTC input, whereas with decoupled HTC inputs, the surface temperature increases nonlinearly as radiation theory predicts. For all vascular materials, the decoupled HTC case exhibits lower surface temperatures than corresponding simulation results for the combined HTC input. This is again related to radiative heat flux loss (q_{rad}) from the exposed top surface that varies nonlinearly with temperature raised to the fourth power (Equation (3)), and thus, becomes more prominent at higher heat fluxes. On the other hand, the combined HTC case results in a linear increase in average top surface temperature with respect to applied heat flux (Equation (6)). Radiation effects are also responsible for the smaller differences in average top surface temperature between the combined and decoupled HTC cases for materials with increasing thermal conductivity. Radiation effects are also responsible for the smaller differences in average top surface temperature between the combined and decoupled HTC cases for materials with increasing thermal conductivity. As shown in **Fig. 9**, In718 with the highest thermal conductivity most effectively advects heat to the liquid coolant within the vasculature and therefore results in a lower average top surface temperature than GFRP/CFRP. This in turn, leads to a lesser contribution of nonlinear radiative heat loss and accordingly the smallest difference in average top surface temperatures between the combined and decoupled HTC simulation cases (Fig. 8c).

This preceding study required a parametric sweep of simulations to be carried out for each material and for each vascular design. Though, the underlying physical phenomenon as well as the governing equations and the boundary conditions are the same in each case. Thus, the problem is naturally suited for a scaling study across some of the governing parameters. Such scaling would help establish an equivalence among the various material systems, thereby eliminating the need to conduct repetitive simulations. The following section presents a dimensional analysis framework for such a scaling across material systems. In the process, the section also establishes another advantage of the decoupled over the combined HTC approach.

5. Non-dimensionalization for temperature field transfer

As laid out in the previous sections, an energy balance for the model thermal regulation system (Fig. 1) is attained through a combination of conduction, natural convection and radiation. During vascular fluid-flow within the system, there is also a thermal energy balance between the heat lost by the host solid along the inner wall of the vasculature and that gained by the coolant sequestered within. These physical phenomena are built into the ROM [10] through appropriate governing differential equations, jump conditions and boundary conditions. The equations that corresponding to the energy balance are:

$$-t\ \mathrm{div}[\kappa\ \mathrm{grad}[T]] = q_{in} - h_{conv}(T - T_{amb}) - \epsilon\sigma(T^4 - T_{amb}^4), \tag{11}$$

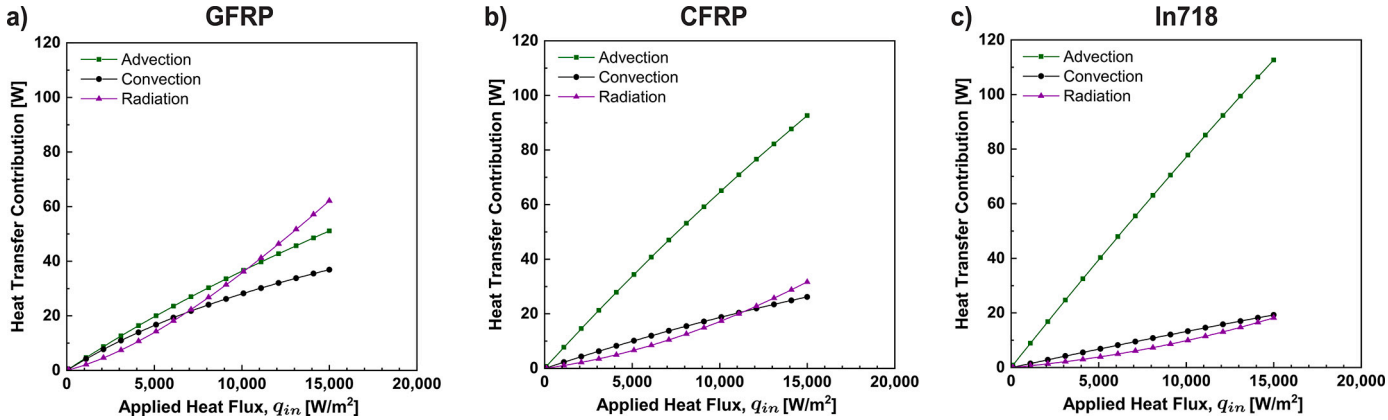

Fig. 9. Contributions from different heat transfer components (i.e., coolant advection, top surface convection, and radiation) at varying applied heat fluxes for vascular: **(a)** GFRP, **(b)** CFRP, and **(c)** In718 containing a branched interconnected network.

and

$$(-\kappa\nabla T\cdot\hat{\mathbf{n}})^{+}+(-\kappa\nabla T\cdot\hat{\mathbf{n}})^{-}=\dot{m}c_f\ \ \nabla T\cdot\hat{\mathbf{t}}, \tag{12}$$

for which $\dot{m}$ is the mass flow rate of the coolant that has a specific heat c_f, $\hat{\mathbf{n}}$ the unit normal away from the solid at the wall of the microchannel, and $\hat{\mathbf{t}}$ the unit tangent on the same surface.

To establish equivalence across material systems of equal thickness (t) and varying host solid thermal conductivity (κ), we begin by defining the characteristic lengths and temperatures as follows:

$$T_{ref}=T_{amb};\qquad \widetilde{T}=T/T_{amb}, \tag{13}$$

$$X_{ref}=L_{ref}, \tag{14}$$

$$Y_{ref}=L_{ref}, \tag{15}$$

$$Z_{ref}=t \tag{16}$$

in which $\widetilde{T}$ denotes a non-dimensional form of T. We will use a similar notation to denote non-dimensional forms in the rest of the paper.

Then the non-dimensional form of the spatial gradient reads:

$$\widetilde{\nabla}=L_{ref}\nabla \tag{17}$$

Substituting these five relations into Equations (11) and (12) gives the following equivalent set of differential equations in terms of non-dimensionalized temperature:

$$-t\frac{\kappa}{h_{conv}L_{ref}^2}\widetilde{\nabla}\widetilde{T}=\frac{q_{in}}{h_{conv}T_{ref}}-(\widetilde{T}-1)-\left(\frac{\epsilon T_{ref}^3}{h_{conv}}\right)\sigma(\widetilde{T}^4-1), \tag{18}$$

and

$$\left(-\kappa\frac{T_{ref}}{L_{ref}}\widetilde{\nabla}\widetilde{T}\cdot\hat{\mathbf{n}}\right)^{+}+\left(-\kappa\frac{T_{ref}}{L_{ref}}\widetilde{\nabla}\widetilde{T}\cdot\hat{\mathbf{n}}\right)^{-}=\dot{m}c_f\frac{T_{ref}}{L_{ref}}\widetilde{\nabla}\widetilde{T}\cdot\hat{\mathbf{t}}. \tag{19}$$

Equations (18) and (19) are essentially the same as Equations (11) and (12), respectively, only differing in the coefficients associated with each term where the difference arises from the process of non-dimensionalization. In other words, Equations (18) and (19) applied to any two vascular material systems will result in solutions that are only scaled by these coefficients. If the parameters that appear in these coefficients are known for a given material system, a combination of parameters can be chosen for another material system to result in the same value of these coefficients, thus establishing equivalence between the two material systems. That is, if we consider two material systems, with material system #1 characterized by $\kappa^{(1)}$, $h_{conv}^{(1)}$, $\epsilon^{(1)}$ and material system #2 by $\kappa^{(2)}$, $h_{conv}^{(2)}$, $\epsilon^{(2)}$, the solution to the boundary value problem for material system #1 with $T_{amb}^{(1)}$, $q_{in}^{(1)}$, $L_{ref}^{(1)}$, and $\dot{m}^{(1)}$ will correspond to the solution for material system #2 with $T_{amb}^{(2)}$, $q_{in}^{(2)}$, $L_{ref}^{(2)}$, and $\dot{m}^{(2)}$. Through this process, we arrive at the following set of equivalent parameters (Table 1) that ensure the non-dimensionalized temperature field is identical between two vascular material systems of equal thickness and varying thermal conductivity.

Table 1
Heat transfer scaling relations across materials systems based on non-dimensionalization.

System Parameters	Scaling Across Material Systems
T_{ref} (temperature)	$T_{ref}^{(2)}\leftarrow\left(\frac{\epsilon^{(1)}}{\epsilon^{(2)}}\frac{h_{conv}^{(2)}}{h_{conv}^{(1)}}\right)^{1/3}T_{ref}^{(1)}$
q_{in} (heat flux)	$q_{in}^{(2)}\leftarrow\left(\frac{h_{conv}^{(2)}}{h_{conv}^{(1)}}\frac{T_{ref}^{(2)}}{T_{ref}^{(1)}}\right)q_{in}^{(1)}$
t (time)	$t^{(2)}\leftarrow t^{(1)}$
L_{ref} (length)	$L_{ref}^{(2)}\leftarrow\left(\frac{h_{conv}^{(1)}}{h_{conv}^{(2)}}\frac{\kappa^{(2)}}{\kappa^{(1)}}\right)^{1/2}L_{ref}^{(1)}$
$\dot{m}$ (mass flow rate)	$\dot{m}^{(2)}\leftarrow\frac{\kappa^{(2)}}{\kappa^{(1)}}\dot{m}^{(1)}$

To further simplify the results, we assume that the emissivity does not vary with scaling. The reason for this assumption is that we would not wish to obtain unreasonable values of emissivity after scaling, especially when we observe from our experiments that the emissivity values for the as-fabricated composite (GFRP and CFRP) surfaces, and for a matte black painted additively manufactured metal (In718) surface are similar. Another simplification that can be made based on the HTC values presented earlier (Fig. 5) is that h_{conv} remains approximately the same across materials. This is consistent with theoretical underpinnings whereby the convective HTC is not a material property, but rather a function of solid geometry and orientation relative to the fluid flow, and the nature of the flow (i.e., laminar/turbulent). Under these two assumptions of constant emissivity and constant h_{conv} across materials, the scaling simplifies to two governing parameters, namely the characteristic length of the solid (L_{ref}) and the mass flow rate of the coolant ($\dot{m}$), as given by Equations (20) and (21), respectively, as follows:

$$L_{ref}^{(2)}\leftarrow\left(\frac{\kappa^{(2)}}{\kappa^{(1)}}\right)^{1/2}L_{ref}^{(1)}, \tag{20}$$

and

$$\dot{m}^{(2)}\leftarrow\frac{\kappa^{(2)}}{\kappa^{(1)}}\dot{m}^{(1)}. \tag{21}$$

All other parameters (i.e., T_{ref}, q_{in}, t) remain identical between the two material systems.

There are two important observations that can be made from these results. First, the scaling shows that equivalent thermal response between two actively-cooled vascular material systems cannot be achieved by varying the coolant flow rate alone. One would also need to vary the characteristic length (i.e., the dimensions of the plate) in addition to the flow rate to be able to replicate the behavior of a reference material system. Second, the equivalence can only be established under the de-

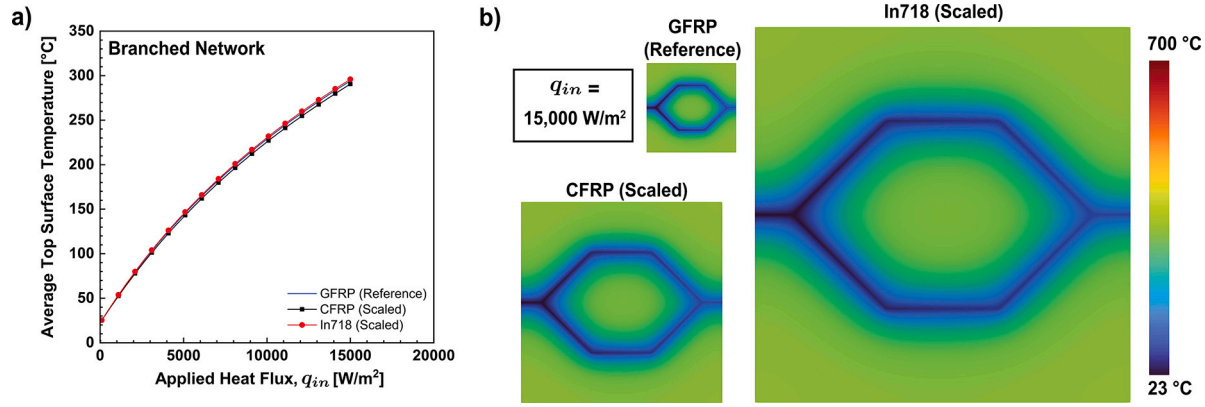

Fig. 10. Illustration of equivalence across material systems based on non-dimensionalization. **(a)** Average top surface temperature versus applied heat flux for GFRP (reference) and equivalently scaled CFRP and In718 results obtained from active-cooling simulations for the branched vascular network with decoupled HTC inputs. (Note: small differences arise from measurement variability and numerical errors.) **(b)** Corresponding cold steady-state (CSS) temperature contours at an applied heat flux of 15,000 W/m^2 for GFRP and equivalently scaled CFRP and In718 material systems.

coupled HTC description. Such a scaling for the temperature field does not exist if a combined HTC is used in Equation (11), further bolstering the case for our theoretically consistent decoupled approach.

Fig. 10 validates this scaling equivalence versus numerical simulations for all three materials with branched vasculature. The analysis considers a square GFRP plate with sides of 100 mm, actively cooled at a flow rate ($\dot{m}$) of 10.17 mL/min, as the reference material platform. Equivalent CFRP and In718 thermal systems are then arrived at by scaling the panel dimensions and coolant flow rate based on the scaling relations established in Equations (20) and (21). The equivalent dimensions for CFRP and In718 are 225 mm and 420 mm, respectively, and the corresponding equivalent flow rates are 51.3 mL/min and 179.1 mL/min, respectively. The three systems are then analyzed numerically using the ROM across a range of heat fluxes. A comparison of the response of the scaled material systems *viz-a-viz* the reference GFRP material platform shows that the same mean surface temperature is achieved in all three materials, within experimental/numerical error (Fig. 10a). The equivalence in thermal response also extends to the point-wise surface temperatures across all three materials (Fig. 10b). The ability to construct such equivalent thermal systems across materials is made possible by the process of self-similarity [54,55], which in turn can only be realized using the decoupled HTC approach as convection and radiation are distinct phenomena.

6. Conclusion

This paper presents (i) a theoretically consistent framework for predicting heat transfer in microvascular materials, particularly in thermal environments outside normal laboratory conditions where measurements are often taken, (ii) ramifications of heat transfer coefficients (HTCs) on thermal regulation, and (iii) a scaling law capturing the active-cooling behavior. To develop the referred framework, we deviate from the status quo and avail the decoupling of convective and radiative components to measure the convective HTC instead of the commonly used combined HTC. The convective HTC can be accurately estimated from the slope of a least-squares fit between the applied heat flux and the change in temperature (for varying heat fluxes); at the same time, the radiative component is well-captured by the classical Stefan-Boltzmann law by measuring emissivity. At low heat fluxes (in a nearly linear regime), active-cooling simulations using experimentally derived inputs reveal good agreement between the combined and decoupled HTC scenarios. However, at higher heat fluxes (i.e., higher surface temperatures), discrepancies between combined and decoupled cases become more pronounced due to increased nonlinear radiation effects. Taking advantage of the decoupled approach, we establish a scaling strategy to transfer the solution fields (e.g., temperature) across material systems. This scaling is possible only under the decoupled HTCs—and not when combined, further strengthening the case for our approach.

The salient features of this work are:

[S1] A theoretically consistent decoupled HTC measurement technique that will improve computational models' accuracy and predictive capabilities by better capturing the underlying physical phenomena.
[S2] Our scaling strategy can be used to validate simulations/experiments across material systems and in different temperature regimes.
[S3] These developments provide not only new capabilities for studying thermal regulation in microvascular materials systems but also offer a deeper understanding of physical phenomenon.

To delve deeper into vascular thermal regulation—either active cooling or active heating, further explorations beyond this study are warranted. Some research questions include:

[Q1] How do spatial non-uniformity in the heat source, ambient and coolant temperature variations, and temperature-dependent material properties of host solid/fluid affect heat transfer behavior? Notably, how do they affect HTC measurements?
[Q2] How significant are the boundary heat losses through the insulation? How can we quantify these losses? And how might they affect HTC measurements and active-cooling behavior?
[Q3] Finally, can these tools (convection-radiation split, measurement protocols, and scaling) be extended to extreme environments (e.g., hypersonic flight paths) to address current obstacles of global importance?

The work presented in this paper furnishes the foundation necessary to pursue answers to the above queries.

CRediT authorship contribution statement

Urmi Devi: Investigation, Formal analysis, Visualization, Writing. **Sandeep R. Kumar:** Investigation, Formal analysis, Visualization, Writing. **Kalyana B. Nakshatrala:** Conceptualization, Methodology, Investigation, Software, Formal Analysis, Writing. **Jason F. Patrick:** Conceptualization, Methodology, Investigation, Project Administration, Funding acquisition, Writing.

Declaration of competing interest

The authors declare the following financial interests/personal relationships which may be considered as potential competing interests: Jason F. Patrick reports financial support was provided by the Air Force Office of Scientific Research.

Data availability

Data will be made available on request.

Acknowledgements

J.F.P acknowledges the support from the Air Force Office of Scientific Research (grant number FA9550-18-1-0048). K.B.N thanks the University of Houston for financial support and computing resources. The authors express their gratitude to NCSU faculty/students: Dr. Ola Harrysson and Satya Konala for help with additive manufacturing of the microvascular metal (In718), and Dr. Jun Liu and Ankit Negi for thermal conductivity measurements of In718.

Appendix A. Supporting information

A.1. Hot steady-state (HSS) experiments

For the HSS experiments, we heated the flat plate samples (at varying applied heat fluxes) using a polyimide thin film resistive heater substrate (Omega, part # KH608/2). The bottom surface of each sample was bonded to a copper base plate (100 x 100 x 6.35 mm) using thermal grease (Parker Chomerics, T670 Thermal grease, part #65-00-T670-0080-DK). The high thermal conductivity of copper (390.84 W/(m·K)) ensures a more uniform heat flux to the bottom surface of the samples. The lateral boundaries of the sample, base plate, and heater assembly were insulated with 5 mm thick chloroprene rubber foam. The bottom of the entire assembly was also insulated with two layers of balsa wood totaling 25.4 mm thickness. The top surface of the sample remains free to convect and radiate heat to the surroundings. The top surface temperature was recorded using an overhead-mounted infrared (IR) camera (FLIR, model # A655sc) with a published accuracy of ± 2°C, and the ambient temperature was recorded using a K-type thermocouple (Phidgets, part # TMP4103_0) with a maximum error rating of 0.75°C, placed at the same height as the IR camera lens (≈ 400 mm away from the heated assembly to avoid interference with the rising natural convective current). The thermal experiments were performed until the average top surface temperature measured by the IR camera reached the HSS condition, i.e., when the temperature did not change by more than 0.2°C over a 10 minute period, as shown in **Fig. A.1**. Ambient temperatures were recorded for the entire duration of the experiment, and the average ambient temperature (T_{amb}) was calculated using the thermocouple reading over the same 10-minute HSS period.

A.2. Discrete versus sequential heating

We conducted HSS experiments with (discrete) and without (sequential) a cool down period in between successive experiments. The discrete HSS experiments were allowed to cool completely to ambient before starting the next experiment. **Fig. A.2a** shows the temperature measurements versus time for an applied heat flux of 1000 W/m^2 for a non-vascular CFRP composite, and the time required (≈ 4 h) for the top surface to cool down to ambient temperature. To ensure cooling of the entire thermal assembly, we conducted only one experiment per day which was time consuming.

To increase experimental throughput, we also conducted HSS experiments on CFRP with sequential heating, where ascending heat fluxes were applied and the sample assembly was not cooled to ambient temperature in between successive experiments (Fig. A.2b). Since we only evaluate the steady-state performance, a cool down period between successive experiments with increasing heat fluxes is not necessary, which saves time and resources. With sequential (i.e., ascending) heating, five experiments could be performed in one day. However, if the heat fluxes are applied in descending order, a cool down to ambient temperature between successive experiments would be required.

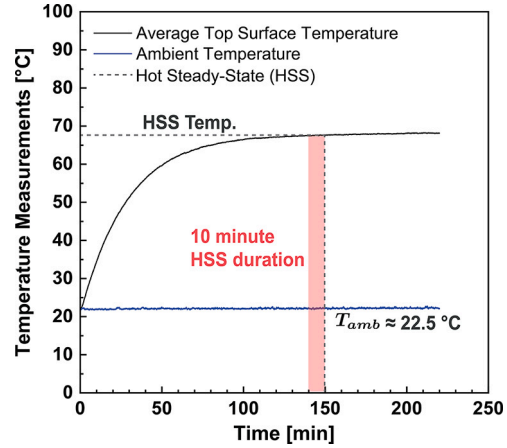

Fig. A.1. Representative transient average top surface and ambient temperatures obtained from the infrared (IR) camera and thermocouple measurements, respectively. The shaded region depicts the hot steady-state (HSS) 10-minute duration.

To evaluate the repeatability of our HSS measurements, we conducted three repeat experiments at each applied heat flux for both discrete and sequential heating. As shown in Fig. A.2a, the average top surface temperatures from three discrete heating experiments are nearly identical, and similar steady-state behavior was observed for the sequential procedure. To compare the reliability of discrete and sequential HSS procedures in calculating the convective HTC (h_{conv}), we plotted convective heat flux (q_{conv}) versus ΔT in Fig. A.2c. The slope of the linear least-squares fit of the corresponding data provides the h_{conv} values for discrete (13.96 ± 0.10 W/(m^2·K)) and sequential (14.05 ± 0.10 W/(m^2·K)) heating, with less than < 1.5% difference. Moreover the standard deviations for both measurement procedures was less than < 0.7%, thereby reinforcing our experimental precision achieved.

The data used to estimate h_{conv} from HSS experiments (Section 3) was obtained from sequential experiments, while the active cooling study (Section 4) was conducted using discrete experiments to calibrate the peristaltic pump to the target coolant flow rate before the start of each experiment.

A.3. Emissivity measurement

The surface emissivity (ϵ) of each sample material (i.e., *unpainted*: GFRP, CFRP composites; *painted*: In718, Cu110 metals) was determined at HSS according to the ASTM standard [46] using a reference emitter (i.e., 3M® Scotch™ Super33+™ vinyl electrical tape) that has a known emissivity of 0.95. To measure the sample surface emissivity, first, two small (≈ 20 x 20 mm) and closely spaced (≈ 5 mm) regions were selected on the top surface that exhibit the same average surface temperature in the IR camera viewport for a fixed emissivity value of ϵ = 0.95. Then, a piece of the reference emitter (i.e., electrical tape) was placed over one region of interest (ROI), as shown in **Fig. A.3a**. After placing the tape, we waited until the reference emitter temperature contour visually reached equilibrium (≈ 1 min). Then, the emissivity of the sample region of interest (ROI) was adjusted until the average top surface temperature matched that of the reference ROI (Fig. A.3b). During this calibration process, we recorded five emissivity measurements within the 10-minute HSS period and report the average value as the final emissivity for each applied heat flux.

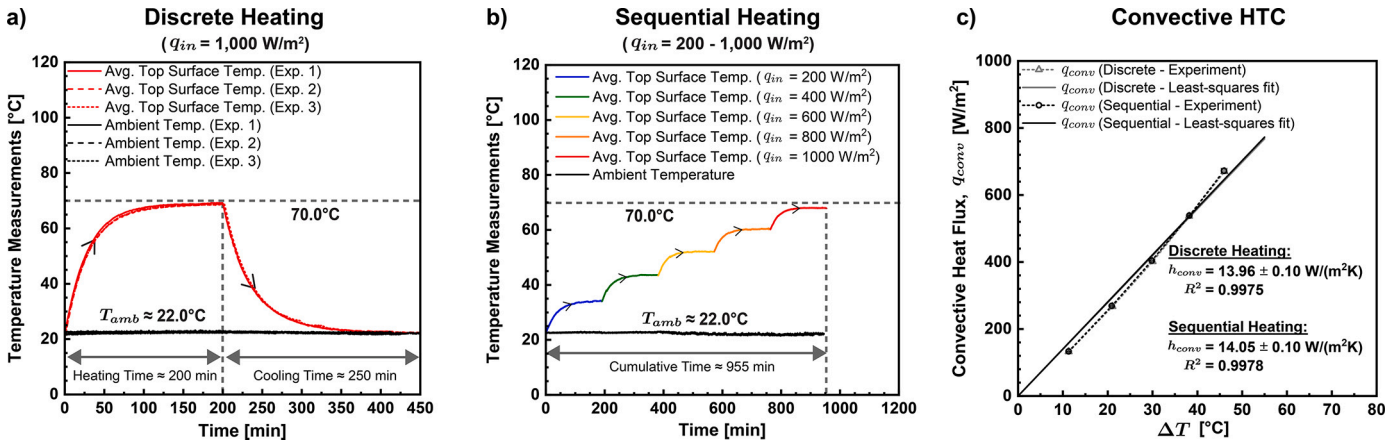

Fig. A.2. Average top surface and ambient temperatures versus time from: **(a)** three discrete HSS experiments conducted on a plain CFRP composite at an applied heat flux of 1000 W/m^2 and **(b)** sequential HSS experiments for the same CFRP composite at applied heat fluxes from 200 to 1000 W/m^2 in 200 W/m^2 increments. **c)** Comparison of the convective heat transfer coefficient (h_{conv}) for discrete and sequential studies via the least-squares fit of q_{conv} versus ΔT. (Note: both x- and y-error bars are plotted, which represent the standard deviation from three experiments conducted on the same sample.)

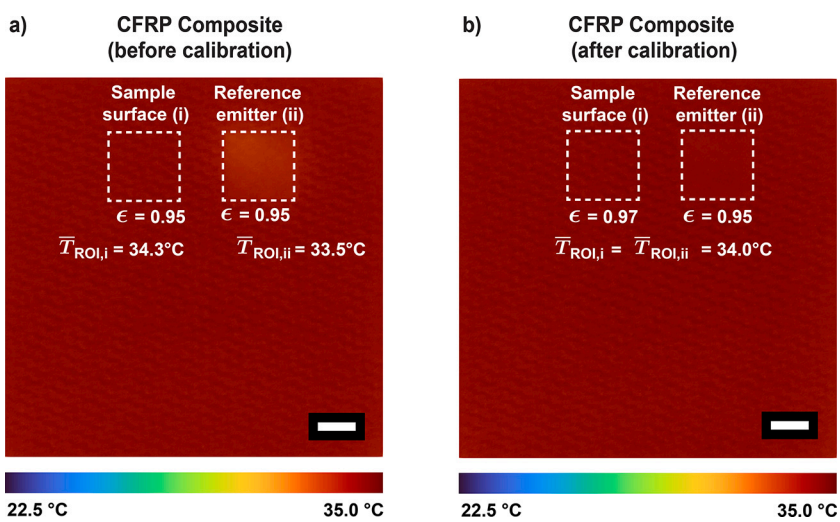

Fig. A.3. Hot steady-state (HSS) temperature contours for a plain CFRP composite at an applied heat flux of 200 W/m^2 showing dashed sample regions of interest (ROIs) without (i) and with (ii) the reference emitter (i.e., electrical tape): **(a)** before emissivity calibration and immediately after the placement of reference emitter and **(b)** after adjusting the CFRP composite sample emissivity to match the reference ROI average top surface temperature (scale bars = 10 mm).

A.4. Effect of vasculature on surface measurements

To investigate the effect of internal vasculature on convective HTC (h_{conv}) measurements, we applied the same methodology to a plain (non-vascular) GFRP composite and a vascularized GFRP composite. A dense serpentine vasculature with 6 mm channel spacing [12] was selected for this study since it has a higher void volume fraction (≈ 0.8%) than either the sinusoidal or the branched vascular samples (≈ 0.1%) presented in this work, and therefore represents a more conservative control. **Figs. A.4a** and **A.4b** show a plain (i.e., non-vascular) GFRP composite and also a GFRP composite with a serpentine vascular template embedded, respectively. Both samples underwent elevated temperature exposure as prescribed by the vaporization of sacrificial components (VaSC) process (Section A.5) to ensure a proper comparison, though only the sample containing the serpentine template produced internal voids.

We conducted HSS experiments on both sample types with the same boundary conditions and applied heat fluxes (i.e., 200, 400, 600, 800, and 1000 W/m^2) as discussed in Sections A.1-A.3. Fig. A.4c shows the resulting convective HTC (h_{conv}) and emissivity (ϵ) values for plain and vascular GFRP composites; h_{conv} differs by less than 3% relative to the plain composite, while ϵ varies by less than 0.5%. Since convection is primarily influenced by the fluid flow conditions of the surrounding environment and radiation depends largely on surface emissivity, the presence of internal vasculature within the composite (at this volume fraction) does not significantly alter h_{conv} or ϵ.

A.5. Microvascular composite fabrication

To fabricate the microvascular glass- and carbon- fiber-reinforced polymer (FRP) composites, we first 3D printed the sinusoidal and branched vascular designs (**Fig. A.5**) from sacrificial poly(lactic) acid (PLA) [50], which were then placed in the mid-plane of each composite fiber preform. Specifically, for GFRP composites, the sacrificial templates were placed atop the 9th layer in a $[90/0]_9$ layup of eight-harness (8H) satin weave E-glass fabric (Style 7781, Fibre Glast Developments Corp.). For the CFRP composites, the sacrificial templates were placed atop the 6th layer of $[90/0]_6$ 8H satin weave carbon-fabric (Style 94407, BGF Industries) stack. Different ply counts were chosen to ensure equivalent thicknesses of each composite type. Note: [0] and [90] represent the warp and weft directions respectively, for the 8H satin woven fabrics.

Epoxy-resin (Araldite LY/Aradur 8605, 100:35 by wt., Huntsman Advanced Materials LLC) was infused into both GFRP and CFRP com-

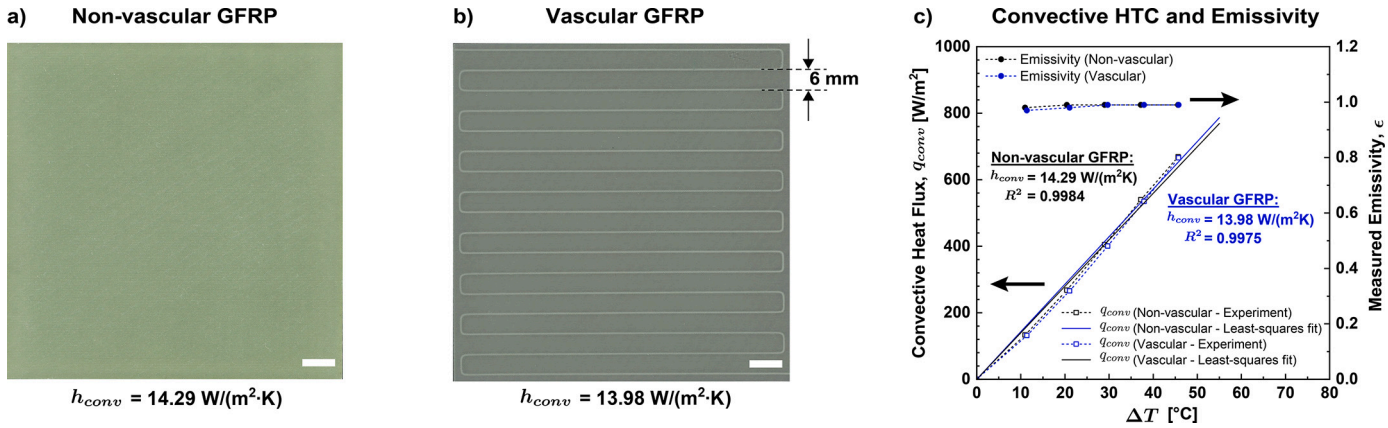

Fig. A.4. **(a)** Plain (i.e., non-vascular) GFRP composite plate. **b)** GFRP composite plate with embedded sacrificial serpentine template at 6 mm channel spacing (scale bars = 10 mm). **(b)** Comparison of convective heat transfer coefficient (h_{conv}) and measured emissivity (ϵ) values at different applied heat fluxes (i.e., 200, 400, 600, 800, and 1000 W/m^2).

posite reinforcement preforms using vacuum assisted resin transfer molding (VARTM) at 2 Torr (abs.) until complete fabric wetting. The vacuum pressure was then reduced to 380 Torr (abs.) and held for 24 h at room temperature (RT) until resin solidification. Afterwards, vacuum was released and the composites were post-cured in forced convection oven for 2 h @ 121°C followed by 2 h @ 150°C to produce a glass-transition temperature (T_g) of approximately 145 °C as measured by dynamic mechanical analysis (DMA). This ensures no warping occurs during the thermal experiments for the prescribed heat fluxes and resulting temperatures (maximum of 110°C) in this study. Composite samples were then cut to the areal dimensions of 100 x 100 mm using a diamond-blade wet-saw, exposing vascule cross-sections. Compressed air-dried composite samples then underwent the vaporization of sacrificial components (VaSC) process [50] in a vacuum oven at 200 °C under ≈ 10 Torr (abs.) of vacuum for 12 h to remove the PLA templates and create micro-channels approximately 500 ± 20 μm in diameter.

A.6. Additive microvascular metal fabrication

To fabricate the microvascular metal samples, additive manufacturing equipment (EOSINT M 280) based on selective laser melting (SLM) [52] was employed to construct the vascular designs (Fig. A.5) within a nickel-chromium superalloy, Inconel 718 (In 718). SLM leverages a high power laser (200 W) to selectively melt and fuse metallic powders successively spread in thin layers on top of a build platform. After completing the SLM fabrication, the sample (still attached to the build platform) was taken out of the machine and the entire assembly was cleaned to remove any residual metal powder via manual vibration/tapping followed by purging the micro-channels with compressed air. This process was repeated until no further metal powder could be extracted. Since localized laser heating/melting from SLM introduces residual stresses, prior to extracting the sample from the build platform, the entire assembly was heat treated in a furnace at ≈ 950°C for 1 h followed by natural cooling inside the furnace. To minimize oxide formation, the furnace was initially purged with argon gas at a high flowrate of ≈ 20 mL/min and then at a lower flowrate (≈ 5 mL/min) for the remaining heat treatment. After relieving the residual stresses via heat treatment, the sample was extracted via wire electrical discharge machining (EDM) and finished via computer numerical control (CNC) machining to the final areal geometry of 100 x 100 mm and a thickness of ≈ 4.5 mm.

A.7. Volumetric flow rate measurement

In order to remain within the laminar flow regime for coolant delivery, which is one assumption of the reduced-order model (ROM) [10]

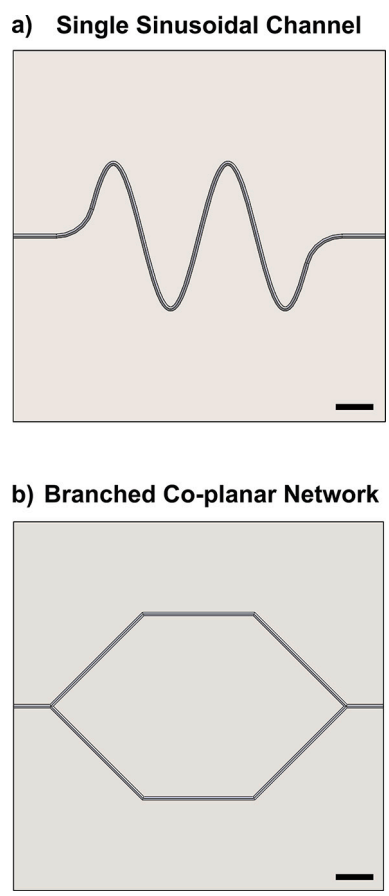

Fig. A.5. Schematics of internal vasculature for active cooling experiments and simulations: **(a)** single sinusoidal channel and **(b)** branched coplanar network (scale bars = 10 mm).

used in this work, a flow-rate calibration study was performed. Similar to prior work [12], Hagen-Poiseuille flow was assumed [56], where the pressure drop (ΔP) is related to the volumetric flow rate (Q) by:

$$\Delta P = Q\frac{128\ \mu L}{\pi D^4}, \tag{A.1}$$

where the constant of proportionality is a function of the fluid viscosity (μ), the channel length (L), and the channel diameter (D) raised to the fourth power.

To generate the flow rate versus pressure drop calibration curves for the microvascular designs in this study, a fluid dispensing unit

Table A.1
Parameters used in the steady-state heat transfer simulation.

Parameter	GFRP		CFRP		In718	
	Sinusoidal	Branched	Sinusoidal	Branched	Sinusoidal	Branched
Length, L [mm]	99.95	99.91	99.9	100.53	99.97	100.04
Width, W [mm]	100.3	100.17	100.31	99.77	100	100.06
Emissivity, ϵ	0.99		0.97		0.94	
Combined HTC from least-squares fit, h_{comb} [W/(m^2·K)]	21.28		21.01		19.81	
Solid in-plane thermal conductivity, $\kappa_{s,11} = \kappa_{s,22}$ [W/(m·K)]	0.6360		3.2110		11.2	
Applied heat flux, q_{in} [W/m^2]	1000	1000	1000	1000	1000	1000
Volumetric flowrate, Q [mL/min]	10.29	10.17	10.21	10.52	10.48	10.33
Ambient temperature at CSS, T_{amb} [°C]	22.82	22.48	23.07	23.92	23.84	23.62
Coolant inlet temperature at CSS, T_{in} [°C]	22.93	22.38	22.71	23.57	23.43	23.10
Coolant thermal conductivity κ_f [W/(m·K)]	0.6					
Coolant density ρ_f [gm/cc]	1.0					
Coolant specific heat c_{pf} [J/(kg·K)]	4183					

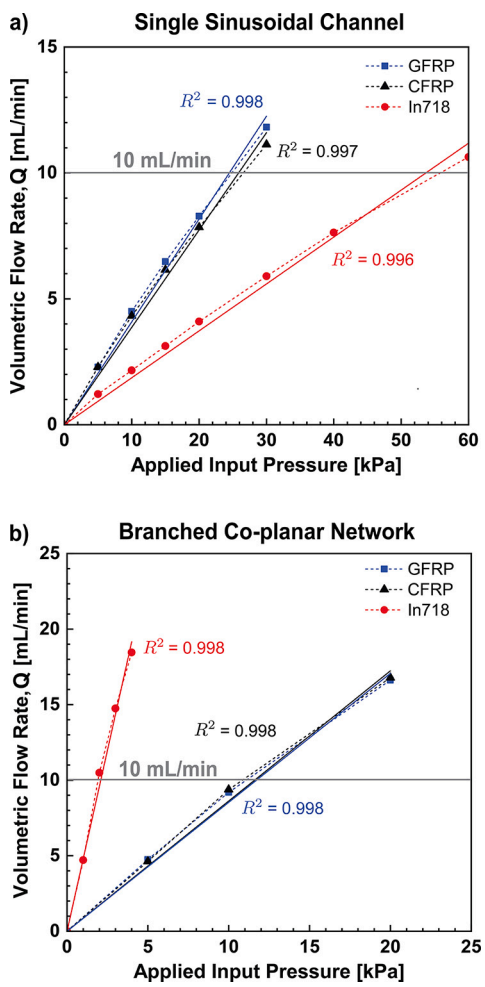

Fig. A.6. Measured volumetric flow rates versus applied input pressures within the laminar flow regime for the: **(a)** single sinusoidal channel and **(b)** branched co-planar network.

(Ultimus V, Nordson EFD) was employed to drive fluid flow via pressure from compressed-air. The inlet/outlet ports on the vascular samples were oversized to 810 μm diameter to reduce connection pressure drop and provide a snug fit for the 21 gauge cylindrical micro-nozzles that were inserted into the channel orifices and connected to the dispensing unit via tubing. The coolant flow-rate was measured by weighing the ejected liquid on a lab balance over a fixed-time interval, for a range of input pressures. The flow-rate versus input pressure curves for both sinusoidal and branched vasculatures are show in **Figs. A.6a** and **A.6b**, respectively. Laminar flow was confirmed via a linear least-squares fit with an R^2 value of at least 0.995. Based on these calibration curves, the prescribed 10 mL/min flow-rate for the peristaltic pump (Cole-Parmer Masterflex, item # EW-07522-30) in the active-cooling experiments was ensured to be laminar.

References

[1] A.M. Coppola, L.G. Warpinski, S.P. Murray, N.R. Sottos, S.R. White, Survival of actively cooled microvascular polymer matrix composites under sustained thermo-mechanical loading, Composites, Part A, Appl. Sci. Manuf. 82 (2016) 170–179.
[2] S.J. Pety, M.H.Y. Tan, A.R. Najafi, P.R. Barnett, P.H. Geubelle, S.R. White, Carbon fiber composites with 2D microvascular networks for battery cooling, Int. J. Heat Mass Transf. 115 (2017) 513–522.
[3] J. Kalirai, Scientific discovery with the James Webb space telescope, Contemp. Phys. 59 (3) (2018) 251–290.
[4] A. Driesman, J. Ercol, E. Gaddy, A. Gerger, Journey to the center of the solar system: how the Parker solar probe survives close encounters with the sun, IEEE Spectr. 56 (5) (2019) 32–53.
[5] M. Moncuquet, N. Meyer-Vernet, K. Issautier, M. Pulupa, J.W. Bonnell, S.D. Bale, T.D. de Wit, K. Goetz, L. Griton, P.R. Harvey, R.J. MacDowall, M. Maksimovic, D.M. Malaspina, First in situ measurements of electron density and temperature from quasi-thermal noise spectroscopy with Parker solar probe/FIELDS, Astrophys. J. Suppl. Ser. 246 (2) (2020) 44.
[6] R. Christen, G. Rizzo, A. Gadola, M. Stöck, Test method for thermal characterization of Li-ion cells and verification of cooling concepts, Batteries 3 (3) (2017).
[7] A.M. Aragón, J.K. Wayer, P.H. Geubelle, D.E. Goldberg, S.R. White, Design of microvascular flow networks using multi-objective genetic algorithms, Comput. Methods Appl. Mech. Eng. 197 (49) (2008) 4399–4410.
[8] S. Soghrati, A.M. Aragón, C. Armando Duarte, P.H. Geubelle, An interface-enriched generalized FEM for problems with discontinuous gradient fields, Int. J. Numer. Methods Eng. 89 (8) (2012) 991–1008.
[9] M.H. Tan, M. Safdari, A.R. Najafi, P.H. Geubelle, A NURBS-based interface-enriched generalized finite element scheme for the thermal analysis and design of microvascular composites, Comput. Methods Appl. Mech. Eng. 283 (2015) 1382–1400.
[10] K.B. Nakshatrala, Modeling thermal regulation in thin vascular systems: a mathematical analysis, Commun. Comput. Phys. 33 (2023) 1035–1068.
[11] K.B. Nakshatrala, K. Adhikari, Modeling thermal regulation in thin vascular systems: a sensitivity analysis, arXiv:2303.0670, https://arxiv.org/abs/2303.0670, 2023.
[12] U. Devi, R. Pejman, Z.J. Phillips, P. Zhang, S. Soghrati, K.B. Nakshatrala, A.R. Najafi, K.R. Schab, J.F. Patrick, A microvascular-based multifunctional and reconfigurable metamaterial, Adv. Mater. Technol. 6 (11) (2021) 2100433.
[13] R. Pejman, S.H. Aboubakr, W.H. Martin, U. Devi, M.H.Y. Tan, J.F. Patrick, A.R. Najafi, Gradient-based hybrid topology/shape optimization of bioinspired microvascular composites, Int. J. Heat Mass Transf. 144 (2019) 118606.
[14] R. Pejman, V. Keshavarzzadeh, A.R. Najafi, Hybrid topology/shape optimization under uncertainty for actively-cooled nature-inspired microvascular composites, Comput. Methods Appl. Mech. Eng. 375 (2021) 113624.
[15] M.H.Y. Tan, A.R. Najafi, S.J. Pety, S.R. White, P.H. Geubelle, Multi-objective design of microvascular panels for battery cooling applications, Appl. Therm. Eng. 135 (2018) 145–157.
[16] A.M. Aragón, R. Saksena, B.D. Kozola, P.H. Geubelle, K.T. Christensen, S.R. White, Multi-physics optimization of three-dimensional microvascular polymeric components, J. Comput. Phys. 233 (2013) 132–147.

[17] A. Bejan, Convection Heat Transfer, 4th edition, John Wiley & Sons, Inc., Hoboken, NJ, 2013.
[18] Y. Çengel, A. Ghajar, Heat and Mass Transfer: Fundamentals and Applications, 6th edition, McGraw Hill, New York, 2014.
[19] J.H. Lienhard IV, J.H. Lienhard V, A Heat Transfer Textbook, 5th edition, Dover Publications, Inc., Mineola, NY, 2019.
[20] M. Milman, W. Petrick, A note on the solution to a common thermal network problem encountered in heat-transfer analysis of spacecraft, Appl. Math. Model. 24 (2000) 861–879.
[21] J.A. Stevenson, J.C. Grafton, Radiation Heat Transfer Analysis for Space Vehicles, (2nd edition), ASD Technical Report 61–119, Part 1, North American Aviation, Inc. for Aeronautical Systems Division, AFSD, US Air Force, Wright Patterson AFB, Ohio, 1961.
[22] J.R. Howell, M.P. Mengüç, K. Daun, R. Siegel, Thermal Radiation Heat Transfer, CRC Press, Boca Raton, FL, 2020.
[23] I. Tiselj, G. Hetsroni, B. Mavko, A. Mosyak, E. Pogrebnyak, Z. Segal, Effect of axial conduction on the heat transfer in micro-channels, Int. J. Heat Mass Transf. 47 (12–13) (2004) 2551–2565.
[24] G.L. Morini, Viscous heating in liquid flows in micro-channels, Int. J. Heat Mass Transf. 48 (17) (2005) 3637–3647.
[25] E. Marín, A. Calderón, O. Delgado-Vasallo, Similarity theory and dimensionless numbers in heat transfer, Eur. J. Phys. 30 (2009) 439.
[26] F.P. Incropera, Convection heat transfer in electronic equipment cooling, J. Heat Transf. 110 (1988) 1097–1111.
[27] T. Fujii, H. Imura, Natural-convection heat transfer from a plate with arbitrary inclination, Int. J. Heat Mass Transf. 14 (1972) 755–767.
[28] E. Radziemska, W.M. Lewandowski, Heat transfer by natural convection from an isothermal downward-facing round plate in unlimited space, Appl. Energy 68 (2001) 347–366.
[29] T.A. Moreira, A.R.A. Colmanetti, C.B. Tibiriçá, Heat transfer coefficient: a review of measurement techniques, J. Braz. Soc. Mech. Sci. Eng. 41 (6) (2019) 1–25.
[30] M. Vollmer, Newton's law of cooling revisited, Eur. J. Phys. 30 (2009) 1063.
[31] J. Fernández-Seara, F.J. Uhía, J. Sieres, A. Campo, A general review of the Wilson plot method and its modifications to determine convection coefficients in heat exchange devices, Appl. Therm. Eng. 27 (2007) 2745–2757.
[32] E. van Rooyen, M. Christians, J.R. Thome, Modified Wilson plots for enhanced heat transfer experiments: current status and future perspectives, Heat Transf. Eng. 33 (2012) 342–355.
[33] X. Zhang, R. Klein, A. Subbaraman, S. Chumakov, X. Li, J. Christensen, C. Linder, S.U. Kim, Evaluation of convective heat transfer coefficient and specific heat capacity of a lithium-ion battery using infrared camera and lumped capacitance method, J. Power Sources 412 (2019) 552–558.
[34] M. Camci, Y. Karakoyun, O. Acikgoz, A.S. Dalkilic, A comparative study on convective heat transfer in indoor applications, Energy Build. 242 (2021) 110985.
[35] R.B. Kennard, An optical method for measuring temperature distribution and convective heat transfer, Langmuir 31(pt (1) (1912) 1229.
[36] D. Naylor, Recent developments in the measurement of convective heat transfer rates by laser interferometry, Int. J. Heat Fluid Flow 24 (2003) 345–355.
[37] G.M. Carlomagno, G. Cardone, Infrared thermography for convective heat transfer measurements, Exp. Fluids 49 (2010) 1187–1218.
[38] V. Narayanan, R.H. Page, J. Seyed-Yagoobi, Visualization of air flow using infrared thermography, Exp. Fluids 43 (2003) 275–284.
[39] G.M. Carlomagno, G. Cardone, C. Meola, T. Astarita, Infrared thermography as a tool for thermal surface flow visualization, J. Vis. 1 (1998) 37–50.
[40] D.A. Aliaga, J.P. Lamb, D.E. Klein, Convection heat transfer distributions over plates with square ribs from infrared thermography measurements, Int. J. Heat Mass Transf. 37 (3) (1994) 363–374.
[41] S. Montelpare, R. Ricci, An experimental method for evaluating the heat transfer coefficient of liquid-cooled short pin fins using infrared thermography, Exp. Therm. Fluid Sci. 28 (2004) 815–824.
[42] D.M. Phillips, M.R. Pierce, J.W. Baur, Mechanical and thermal analysis of microvascular networks in structural composite panels, Composites, Part A, Appl. Sci. Manuf. 42 (11) (2011) 1609–1619.
[43] S. Soghrati, P.R. Thakre, S.R. White, N.R. Sottos, P.H. Geubelle, Computational modeling and design of actively-cooled microvascular materials, Int. J. Heat Mass Transf. 55 (19) (2012) 5309–5321.
[44] M.H.Y. Tan, A.R. Najafi, S.J. Pety, S.R. White, P.H. Geubelle, Gradient-based design of actively-cooled microvascular composite panels, Int. J. Heat Mass Transf. 103 (2016) 594–606.
[45] T.J. Quinn, J.E. Martin, A radiometric determination of the Stefan-Boltzmann constant and thermodynamic temperatures between -40°C and +100°C, Philos. Trans. R. Soc. Lond. Ser. A, Math. Phys. Sci. 316 (1985) 85–189.
[46] ASTM E1933-14, Standard practice for measuring and compensating for emissivity using infrared imaging radiometers, 2018.
[47] P. Jiang, X. Qian, R. Yang Tutorial, Time-domain thermoreflectance (TDTR) for thermal property characterization of bulk and thin film materials, J. Appl. Phys. 124 (16) (2018) 161103.
[48] A. Jarrett, I.Y. Kim, Design optimization of electric vehicle battery cooling plates for thermal performance, J. Power Sources 196 (2011) 10359–10368.
[49] J.C. Kurnia, A.P. Sasmito, A.S. Mujumdar, Numerical investigation of laminar heat transfer performance of various cooling channel designs, Appl. Therm. Eng. 31 (2011) 1293–1304.
[50] J.F. Patrick, B.P. Krull, M. Garg, C.L. Mangun, J.S. Moore, N.R. Sottos, S.R. White, Robust sacrificial polymer templates for 3D interconnected microvasculature in fiber-reinforced composites, Composites, Part A, Appl. Sci. Manuf. 100 (2017) 361–370.
[51] A.P. Esser-Kahn, P.R. Thakre, H. Dong, J.F. Patrick, V.K. Vlasko-Vlasov, N.R. Sottos, J.S. Moore, S.R. White, Three-dimensional microvascular fiber-reinforced composites, Adv. Mater. 23 (32) (2011) 3654–3658.
[52] C.Y. Yap, C.K. Chua, Z.L. Dong, Z.H. Liu, D.Q. Zhang, L.E. Loh, S.L. Sing, Review of selective laser melting: materials and applications, Appl. Phys. Rev. 2 (4) (2015) 041101.
[53] M. Biedermann, P. Beutler, M. Meboldt, Automated design of additive manufactured flow components with consideration of overhang constraint, Addit. Manuf. 46 (2021) 102119.
[54] G.I. Barenblatt, Scaling, Self-Similarity, and Intermediate Asymptotics: Dimensional Analysis and Intermediate Asymptotics, vol. 14, Cambridge University Press, Cambridge, 1996.
[55] M. Bowen, T. Witelski, Methods of Mathematical Modelling Continuous Systems and Differential Equations, Springer Publication, New York, 2015.
[56] B.R. Munson, T.H. Okiishi, W.W. Huebsch, A.P. Rothmayer, Fundamentals of Fluid Mechanics, 7th edition, John Wiley & Sons, Inc., Hoboken, NJ, 2012.